

Playground of Lognormal Seminumerical Simulations of the Lyman α Forest

Thermal History of the Intergalactic Medium

T. Ondro^{1,2}, B. Arya³ and R. Gális⁴

¹ Department of Technology and Automobile Transport, Faculty of AgriSciences, Mendel University in Brno, Zemědělská 1, 613 00 Brno, Czech Republic
e-mail: tomas.ondro@mendelu.cz

² Department of Applied Mathematics, VSB - Technical University of Ostrava, 17. listopadu 15/2172, 70800 Ostrava, Czech Republic

³ Department of Space, Planetary & Astronomical Sciences & Engineering, Indian Institute of Technology, Kanpur 208016, Uttar Pradesh, India
e-mail: bhaskara@iitk.ac.in

⁴ Institute of Physics, Faculty of Science, Pavol Jozef Šafárik University in Košice, Park Angelinum 9, 040 01 Košice, Slovakia
e-mail: rudolf.galis@upjs.sk

Received September 15, 1996; accepted March 16, 1997

ABSTRACT

Aims. This study aims to test a potential application of lognormal seminumerical simulations to recover the thermal parameters and Jeans length. This could be suitable for generating large number of synthetic spectra with various input data and parameters, and thus ideal for interpreting the high-quality data obtained from QSO absorption spectra surveys.

Methods. We use a seminumerical approach to simulate absorption spectra of quasars at redshifts $3 \leq z \leq 5$. These synthetic spectra are compared with the 1D flux power spectra and using the Markov Chain Monte Carlo analysis method we determine the temperature at mean density, slope of the temperature-density relation and Jeans length. Our best-fit model is also compared with the evolution of the temperature of the intergalactic medium from various UVB models.

Results. We show that the lognormal simulations can effectively recover thermal parameters and Jeans length. Besides, by comparing the synthetic flux power spectra with observations from Baryon Oscillation Spectroscopy Survey we found, that such an approach can be also used for the cosmological parameter inference.

Key words. Cosmology: miscellaneous – intergalactic medium – Methods: data analysis – Methods: numerical

1. Introduction

The primary observational evidence for the intergalactic medium (IGM) comes from absorption lines at wavelengths shortward of the Lyman- α (Ly- α) emission line. These are thought to be the Ly- α absorption lines arising from the moderate overdensities ($\Delta \lesssim 10$) in the gas density field (Viel et al. 2002a,b; Demiański et al. 2011). Thus, these absorption lines in the spectra of high redshift sources are being revealed as an extremely powerful tool in observational cosmology (Font-Ribera et al. 2012). For example, the final sample from the extended Baryon Oscillation Spectroscopy Survey (eBOSS) from Chabanier et al. (2019) contains approximately 210,000 quasars (du Mas des Bourboux et al. 2020). This imposes a condition to produce computationally inexpensive, but realistic datasets. For this purpose, it is therefore suitable to use the numerical and semianalytical models for the IGM, which are developing from the 1990s (Bi et al. 1992; Bi 1993; Bi et al. 1995; Bi & Davidsen 1997). Although this is relatively simple model, it can predict various properties of the absorption lines, such as column density distribution and the distribution of linewidths (Viel et al. 2002b).

Nowadays, a majority of studies which are focused on the statistical properties of the Ly- α forest use modern hydrodynamical simulations for interpreting the observations. These simula-

tions are, on the one hand, more accurate and include most of the relevant physics to model the Ly- α forest. On the other hand, they are computationally extensive which is the limitation in the case, when we want to explore large parameter space. Therefore, the efficient semi-numerical models of the Ly- α forest may have an important role in interpreting of the cosmological and astrophysical parameters from QSO absorption spectra surveys.

In the past, many such semi-numerical methods have been proposed, such as: (i) assuming baryons trace a smoothed dark matter density field (Petitjean et al. 1995; Croft et al. 2002), (ii) Taylor expanding the observables around a "best-guess" model interpreted from few hydrodynamic simulations, (iii) semi-analytical modeling using lognormal approximation (Coles & Jones 1991; Hui & Gnedin 1997; Bi & Davidsen 1997; Choudhury et al. 2001; Arya et al. 2023, 2024). Results from these methods show that the Ly- α forest is sensitive to the astrophysical processes in the IGM, thereby marginalizing these astrophysical parameters is imperative to constraining cosmology and dark matter models using the Ly- α forest.

The aim of this study is to test the potential application of lognormal seminumerical simulations to recover the temperature at mean density, slope of the temperature-density relation and Jeans length between $3 \leq z \leq 5$. The lognormal allows us to efficiently generate Ly- α spectra while accounting for non-

Gaussianities in the baryonic density field to a certain extent. We utilise the Ly- α flux power spectrum, which is often used to constrain the thermal (Boera et al. 2019; Walther et al. 2019; Gaikwad et al. 2021) and also the cosmological parameters (McDonald et al. 2000; Viel et al. 2004), to compare the observational results with our model.

The article is organised as follows: Section 2 contains the theoretical background of the lognormal seminumerical simulations of the Ly- α forest. Description of the Ly- α flux power spectrum calculation is presented in Section 3. These two sections are meant to provide a comprehensive description of the methods used in this study, making them fairly technical in nature. Section 4 contains information about observational data and methodology for the Markov Chain Monte Carlo inference used to restore the thermal parameters and Jeans length. In Section 5, we present our results for the best-fit model and the comparison of determined values of temperature at a mean density with the thermal evolution of the IGM. Our conclusions are given in Section 6.

In this study, we used the default cosmological parameters: $(\Omega_\Lambda, \Omega_m, \Omega_b, \sigma_8, n_s, h, Y) = (0.692, 0.308, 0.0482, 0.829, 0.961, 0.678, 0.24)$ consistent with a flat Λ CDM cosmology (Planck Collaboration et al. 2014).

2. Simulating the QSO absorption spectra

In this section, we describe the structure of the lognormal seminumerical model, which is based on previous studies (Choudhury et al. 2001; Arya et al. 2023, 2024). Note that we also provide algorithms for most tricky parts.

We started with linearly extrapolated power spectrum of dark matter (DM) density field $P_{\text{DM}}(k)$ calculated for a given set of cosmological parameters at the present epoch ($z = 0$). In this study, we used the power spectrum as computed by the CAMB Boltzmann solver (Lewis et al. 2000). Then, the 3D power spectrum of the baryonic density fluctuations for any arbitrary z is given by

$$P_B(k, z) = D^2(z) P_{\text{DM}}(k) \exp[-2x_J^2(z)k^2], \quad (1)$$

where $D(z)$ is the linear growth factor and $x_J(z)$ is Jeans length. The algorithm for calculating the aforementioned quantities is listed in Fig. 1.

To simulate the one dimensional density and velocity fields for a chosen redshift z , we start with two independent Gaussian fields $w_0(k)$ and $u_0(k)$ with unit power spectrum. Then, we prepare two independent Gaussian fields with power spectra $P_w(k, z)$ and $P_u(k, z)$ as

$$w(k, z) = w_0(k) \sqrt{P_w(k, z)} \quad (2)$$

and

$$u(k, z) = u_0(k) \sqrt{P_u(k, z)}, \quad (3)$$

where

$$P_w(k, z) = \beta^{-1}(k, z) \frac{1}{2\pi} \int_{|k|}^{\infty} \frac{dk'}{k'} P_B(k', z), \quad (4)$$

$$P_u(k, z) = \frac{1}{2\pi} \int_{|k|}^{\infty} dk' k' P_B(k', z) - P_w(k, z), \quad (5)$$

Input: $P_{\text{DM}}, k, N_{\text{pix}}, x_J, h, \Omega_m, \Omega_k, \Omega_\Lambda, z_{\text{min}}, z_{\text{max}}$

Output: $P_B(k, z), k, k_{\text{val}}, L_{\text{box}}, z$

begin

```

     $z = (z_{\text{min}} + z_{\text{max}})/2$ ;
     $D(z) \leftarrow$  normalized growth factor at redshift  $z$ ;
     $k = k * h$ ; /* h Mpc-1 to Mpc-1 */
     $P_{\text{DM}}(k) = P_{\text{DM}}/h^3$ ; /* (Mpc/h)3 to Mpc3 */
     $P_B(k, z) = D^2(z) P_{\text{DM}}(k) \exp[-2x_J^2(z)k^2]$ ;
     $L_{\text{box}} = \text{COM\_DIST}(z_{\text{max}}) - \text{COM\_DIST}(z_{\text{min}})$ ;
     $dx = L_{\text{box}}/N_{\text{pix}}$ ;
     $d = dx/(2 * \pi)$ ;
     $k_{\text{val}} = [0, 1, \dots, n/2 - 1, -n/2, \dots, -1]/(N_{\text{pix}} * d)$ ;
     $\text{int1} \leftarrow 0$ ;
     $\text{int2} \leftarrow 0$ ;
     $\text{int3} \leftarrow 0$ ;
    for  $i \leftarrow 1$  to  $\text{length}(k) - 1$  do
         $\text{sum1} \leftarrow 0$ ;
         $\text{sum2} \leftarrow 0$ ;
         $\text{sum3} \leftarrow 0$ ;
        for  $j \leftarrow i$  to  $\text{length}(k) - 1$  do
             $\text{sum1} \leftarrow \text{sum1} + \left[ \frac{P_B(k, z)[j]}{k[j]} + \frac{P_B(k, z)[j+1]}{k[j+1]} \right] * \frac{k[j+1] - k[j]}{2}$ ;
             $\text{sum2} \leftarrow \text{sum2} + [P_B(k, z)[j] * k[j] + P_B(k, z)[j+1] * k[j+1]] * \frac{k[j+1] - k[j]}{2}$ ;
             $\text{sum3} \leftarrow \text{sum3} + \left[ \frac{P_B(k, z)[j]}{k[j]^3} + \frac{P_B(k, z)[j+1]}{k[j+1]^3} \right] * \frac{k[j+1] - k[j]}{2}$ ;
        end
         $\text{int1}[i] \leftarrow \text{sum1}$ ;
         $\text{int2}[i] \leftarrow \text{sum2}$ ;
         $\text{int3}[i] \leftarrow \text{sum3}$ ;
    end
     $\beta(k_{\text{val}}, z) \leftarrow \text{INTERP}(k_{\text{val}}, k, \text{int3})/\text{INTERP}(k_{\text{val}}, k, \text{int1})$ ;
     $P_w(k_{\text{val}}, z) \leftarrow \frac{1}{2\pi\beta(k_{\text{val}}, z)} \text{INTERP}(k_{\text{val}}, k, \text{int1})$ ;
     $P_u(k_{\text{val}}, z) \leftarrow \frac{1}{2\pi} \text{INTERP}(k_{\text{val}}, k, \text{int2}) - P_w(k_{\text{val}}, z)$ ;
end

```

Fig. 1. Algorithm for calculating 3D power spectrum of the baryonic density fluctuations. Note that the `COM_DIST` and `INTERP` functions are for the calculation of comoving distance and one-dimensional linear interpolation, respectively.

and

$$\beta(k, z) = \frac{\int_{|k|}^{\infty} (dk'/k'^3) P_B(k', z)}{\int_{|k|}^{\infty} (dk/k') P_B(k', z)}. \quad (6)$$

Then, the linear density and velocity fields in the k -space are given by

$$\delta_B(k, z) = w(k, z) + u(k, z), \quad (7)$$

$$v(k, z) = \dot{a} k \beta(k, z) w(k, z), \quad (8)$$

where \dot{a} is the time derivative of the scale factor

$$\dot{a}^2(z) = H_0^2 \left[\Omega_m(1+z) + \Omega_k + \frac{\Omega_\Lambda}{(1+z)^2} \right], \quad (9)$$

where H_0 is the present expansion rate of the Universe, and Ω_m , Ω_k and Ω_Λ are the cosmological parameters corresponding to the content of matter, curvature and dark energy, respectively. The $\delta_B(x, z)$ and $v(x, z)$ in real comoving space are obtained using Fourier transforms. The algorithm for calculating aforementioned quantities is listed in Fig. 2.

Note that we firstly calculated the Eqs. (4) and (5) from the all values of 3D power spectrum of the baryonic density fluctuations P_B , and then we used interpolation at specific query points as we need the values of P_w and P_u at k_{vals} (see Fig. 1).

Input: $P_w, P_u, k_{\text{val}}, L_{\text{box}}, N_{\text{pix}}, H_0, \Omega_m, \Omega_k, \Omega_\Lambda, z$
Output: $\delta_B(x, z), v(x, z)$
begin
 $w_{\text{re}}, w_{\text{im}}, u_{\text{re}}, u_{\text{im}} \leftarrow 0$; /* arrays of size N_{pix} */
 for $j \leftarrow 2$ **to** $N_{\text{pix}}/2$ **do**
 $w_{\text{re}}[j] = \text{rand1}[j] * \sqrt{P_w[j]/2}$;
 $w_{\text{im}}[j] = \text{rand1}[N_{\text{pix}}/2 + j - 1] * \sqrt{P_w[j]/2}$;
 $u_{\text{re}}[j] = \text{rand2}[j] * \sqrt{P_u[j]/2}$;
 $u_{\text{im}}[j] = \text{rand2}[N_{\text{pix}} + j - 1] * \sqrt{P_u[j]/2}$;
 end
 for $j \leftarrow 1$ **to** $N_{\text{pix}}/2$ **do**
 $w_{\text{re}}[N_{\text{pix}}/2 + j] = w_{\text{re}}[N_{\text{pix}}/2 - j + 2]$;
 $w_{\text{im}}[N_{\text{pix}}/2 + j] = -w_{\text{im}}[N_{\text{pix}}/2 - j + 2]$;
 $u_{\text{re}}[N_{\text{pix}}/2 + j] = u_{\text{re}}[N_{\text{pix}}/2 - j + 2]$;
 $u_{\text{im}}[N_{\text{pix}}/2 + j] = -u_{\text{im}}[N_{\text{pix}}/2 - j + 2]$;
 end
 $\dot{a} = H_0 \sqrt{\Omega_m(1+z) + \Omega_k + \frac{\Omega_\Lambda}{(1+z)^2}}$;
 $\delta_B(k, z) = (w_{\text{re}} + u_{\text{re}}) + i * (w_{\text{im}} + u_{\text{im}})$;
 $v(k, z) = \dot{a} * k_{\text{val}} * \beta(k, z) * (-w_{\text{im}} + i * w_{\text{re}})$;
 $\delta_B(x, z) = \text{IFFT}[\delta_B(k, z)] * N_{\text{pix}}/L_{\text{box}}^3$;
 $v(x, z) = \text{IFFT}[v(k, z)] * N_{\text{pix}}/L_{\text{box}}^3$;
end

Fig. 2. Algorithm for calculating $\delta(x, z)$ and $v(x, z)$. Note that *rand1* and *rand2* are random samples of size N_{pix} from Gaussian distribution of zero mean and unit variance, i is the imaginary unit ($i = \sqrt{-1}$) and the function *IFFT* computes the one-dimensional inverse discrete Fourier transform.

To account the effect of non-linearities, we assuming the number density distribution of baryons n_B to be a lognormal field

$$n_B = A \exp[\delta_B(x, z)], \quad (10)$$

where $\delta_B(x, z)$ is the linear density contrast in baryons. Normalization constant A can be calculated as

$$A = \frac{n_0(z)}{\langle \exp[\delta_B(x, z)] \rangle}, \quad (11)$$

where

$$n_0 = \frac{\Omega_B \rho_C}{\mu_B m_p} (1+z)^3, \quad (12)$$

where ρ_C corresponds to the critical density of Universe, Ω_B is the baryonic density parameter and the term in denominator corresponds to the mass per baryonic particle given by $\mu_B m_p = 4m_p/(4-3Y)$. Combining equations (10) and (11) leads to

$$n_B(x, z) = n_0(z) \frac{\exp[\delta_B(x, z)]}{\langle \exp[\delta_B(x, z)] \rangle}. \quad (13)$$

Under the assumption of photoionization equilibrium,

$$n_{\text{H I}} = \frac{\alpha(T) n_p n_e}{\Gamma_{\text{H I}}(z)}, \quad (14)$$

where $\alpha(T)$ is the recombination coefficient at temperature T , n_p , n_e are the number densities of protons and free electrons, respectively, and $\Gamma_{\text{H I}}$ is the hydrogen photoionization rate. Assuming a fully ionized IGM, number densities of protons and free electrons are given by

$$n_p(x, z) = \frac{4(1-Y)}{4-3Y} n_B(x, z) \quad (15)$$

and

$$n_e(x, z) = \frac{4-2Y}{4-3Y} n_B(x, z), \quad (16)$$

where Y is the helium weight fraction. Note that we take the temperature dependence of $\alpha(T)$ to be given by Rauch et al. (1997)

$$\alpha(T) = 4.2 \times 10^{-13} \left[\frac{T(x, z)}{10^4 \text{K}} \right]^{-0.7}. \quad (17)$$

The temperature field can be related to the baryonic density using the following equation

$$T(x, z) = T_0(z) \left(\frac{n_b(x, z)}{n_0(z)} \right)^{\gamma(z)-1}, \quad (18)$$

where T_0 is the temperature at the mean density and $(\gamma - 1)$ is a power-law index.

The last step is to calculate the transmitted flux according to the equation

$$F = F_c \exp(-\tau), \quad (19)$$

where continuum flux F_c was set up to unity. The Ly- α optical depth is calculated as

$$\tau(x_i, z) = \frac{c I_\alpha}{\sqrt{\pi}} \sum_j \delta x \frac{n_{\text{H I}}(x_j, z)}{b(x_j, z)[1 + z(x_j)]} \times V_\alpha \left(\frac{c[z(x_j - z(x_i))]}{b(x_j, z)[1 + z(x_i)]} + \frac{v_b[x_j, z]}{b(x_j, z)} \right), \quad (20)$$

where i, j corresponds to the indexes of the points along the line of sight (LOS), I_α is the Ly- α absorption cross-section, δx is the separation between the grid points, and V_α is the Voigt profile for the Ly- α transition. The quantity

$$b(x, z) = \sqrt{\frac{2k_b T(x, z)}{m_p}} \quad (21)$$

is the Doppler parameter and k_b is Boltzmann constant. We also plot steps of transformation in Fig. 3.

3. Ly- α flux power spectrum

The Ly- α flux power spectrum is often used to constrain the thermal (Boera et al. 2019; Walther et al. 2019; Gaikwad et al. 2021) and also the cosmological parameters (McDonald et al. 2000; Viel et al. 2004). In this work, we performed the power spectrum measurements on the flux contrast estimator

$$\delta_F = \frac{F(v) - \langle F \rangle}{\langle F \rangle}, \quad (22)$$

where $F(v)$ is the transmission in the Ly- α forest and $\langle F \rangle$ is the mean flux. The transmitted flux power spectrum (FPS) is computed according Villaseñor et al. (2021) as

$$P(k) = v_{\text{max}} \langle |\tilde{\delta}_F(k)|^2 \rangle, \quad (23)$$

where

$$\tilde{\delta}_F(k) = \frac{1}{v_{\text{max}}} \int_0^{v_{\text{max}}} \exp(-iku) \delta_F(v) dv. \quad (24)$$

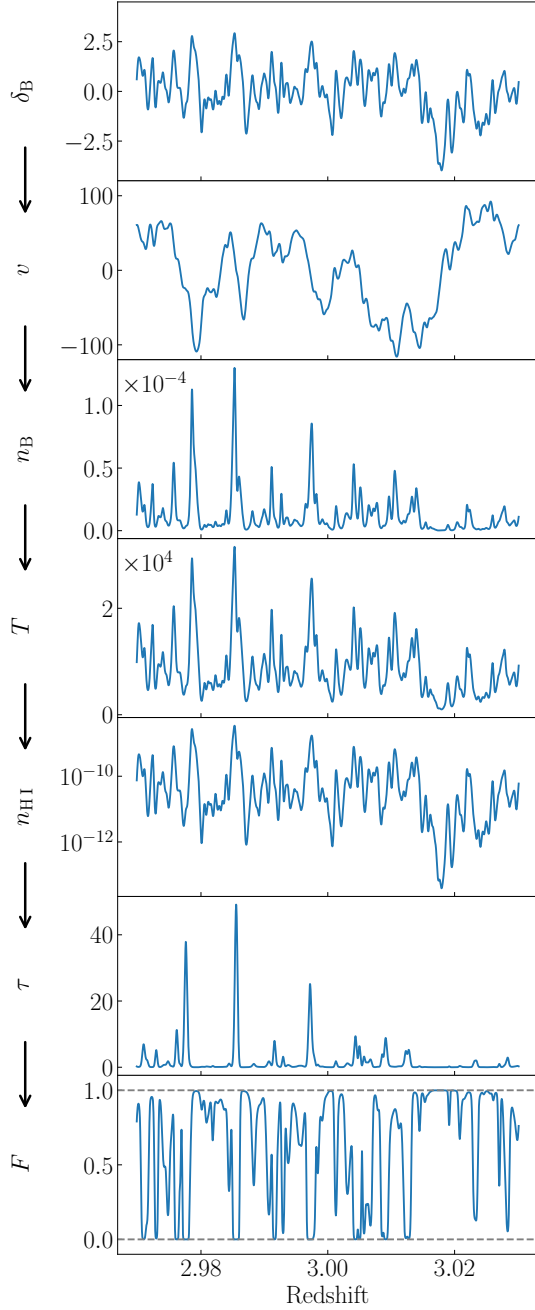


Fig. 3. Sample of one line of sight at different stages of transformation.

The FPS is often expressed in terms of the dimensionless quantity

$$\Delta_F^2(k) = \frac{1}{\pi} k P(k), \quad (25)$$

where $k = 2\pi/v$. The sensitivity of FPS to the parameters T_0 , γ and x_J is shown in Fig. 4. The FPS in our models at scales $k < 0.01$ is nearly the same because of the dark matter density field is the same for all models. It can be also observed that the flux power spectrum is systematically lower for model with higher T_0 at scales $0.03 < k < 0.2$, whereas is lower for models with higher value of γ .

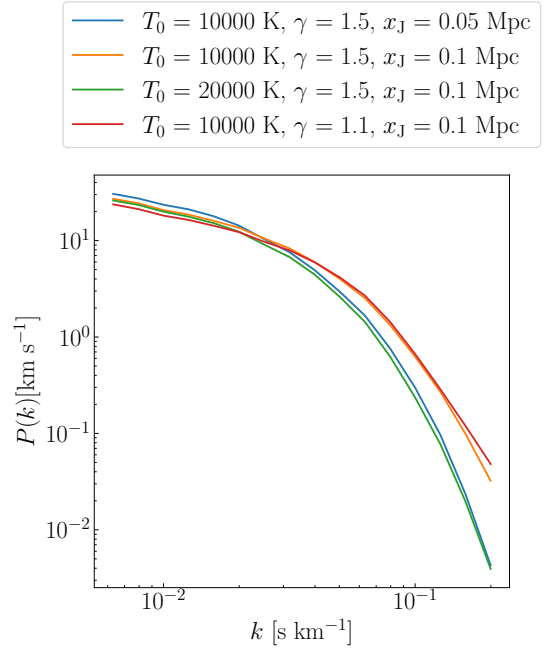


Fig. 4. Sensitivity of FPS to the parameters T_0 , γ and x_J for four models.

4. Observational Data

In this study, we used the observational determinations of the FPS measured from the studies of Iršič et al. (2017) and Boera et al. (2019) for comparison with our models. Note that we also plot the FPS based on the eBOSS measurements (Chabanier et al. 2019). Since this FPS is estimated in the redshift range of $2.2 < z < 4.6$ and probes mostly large scales (corresponds to the interval $0.001 \text{ s km}^{-1} \leq k \leq 0.02 \text{ s km}^{-1}$), we can also test the use of this approach for cosmological parameter inference.

For completeness we add that we do not use the results from the study of Walther et al. (2018) because, as was noted in Villasenor et al. (2022), the estimates show significant differences with those from eBOSS in the overlapping range of scales ($0.003 \text{ s km}^{-1} \leq k \leq 0.02 \text{ s km}^{-1}$). To get closer to the cosmological simulations, in the case of each redshift bin, we used the 1D array of length $40 h^{-1} \text{ Mpc}$ with 2048 elements, which is suitable for studying the small scale structures probed by the Ly- α forest.

We applied the MCMC sampler (Lewis & Bridle 2002; Lewis 2013; Torrado & Lewis 2019, 2021) to compare the simulated $P(k)$ to the observational measurements in the redshift range of $3 \leq z \leq 5$. To determine when a chain is converged, we use Gelman-Rubin statistics parameter, $R - 1 < 0.05$ (Gelman & Rubin 1992).

In the case of thermal parameters, we adopt flat priors on temperature at the mean density T_0 , γ and x_J in the ranges $3000 \text{ K} < T_0 < 20000 \text{ K}$, $0.75 < \gamma < 2.25$, and $0.04 \text{ Mpc} < x_J < 0.4 \text{ Mpc}$, respectively. For the hydrogen photoionization rate Γ_{HI} , we used values from the study of Faucher-Giguère (2020). The likelihood function for the model given by the parameters $\Theta = \{T_0, \gamma, x_J\}$ is evaluated as

$$\ln \mathcal{L}(\Theta) = -\frac{1}{2} \sum_k \left[\left(\frac{P(k) - P_{\text{model}}(k, \Theta)}{\sigma(k)} \right)^2 + \ln 2\pi\sigma(k)^2 \right]. \quad (26)$$

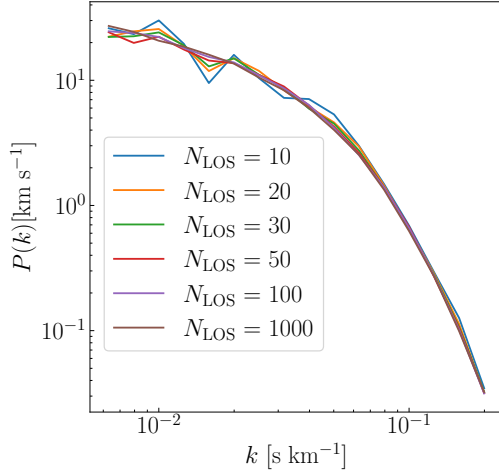


Fig. 5. Illustration of the impact of various LOS number used for the FPS calculation. In this case we used the parameters $T_0 = 10\,000$ K, $\gamma = 1.5$ and $x_J = 0.1$ Mpc.

5. Results and Discussion

5.1. $P(k)$ Model Comparison with Data

The comparison of the best-fit synthetic FPS at various redshifts is shown in Fig. 6 and the parameter estimates obtained from the MCMC runs are presented in Tab. 1 and Appendix A.

Table 1. Values of the determined parameters

| redshift | T_0 [K] | γ | x_J [Mpc] |
|----------|---------------------------|------------------------|---------------------------|
| 3.0 | $16\,746^{+1645}_{-1763}$ | $1.42^{+0.20}_{-0.26}$ | $0.129^{+0.017}_{-0.019}$ |
| 3.2 | $17\,858^{+1395}_{-1893}$ | $1.40^{+0.09}_{-0.09}$ | $0.085^{+0.015}_{-0.011}$ |
| 3.4 | $15\,609^{+1301}_{-1236}$ | $1.53^{+0.07}_{-0.07}$ | $0.079^{+0.012}_{-0.011}$ |
| 3.6 | $18\,115^{+1151}_{-1322}$ | $1.42^{+0.08}_{-0.08}$ | $0.072^{+0.010}_{-0.009}$ |
| 3.8 | $18\,163^{+1267}_{-3055}$ | $1.44^{+0.15}_{-0.37}$ | $0.100^{+0.012}_{-0.008}$ |
| 4.0 | $16\,375^{+2463}_{-2443}$ | $1.15^{+0.24}_{-0.26}$ | $0.094^{+0.008}_{-0.009}$ |
| 4.2 | $8\,370^{+2064}_{-1589}$ | $1.16^{+0.23}_{-0.21}$ | $0.071^{+0.006}_{-0.008}$ |
| 4.6 | $8\,855^{+1756}_{-1461}$ | $1.20^{+0.17}_{-0.15}$ | $0.061^{+0.003}_{-0.004}$ |
| 5.0 | $10\,870^{+2017}_{-2267}$ | $1.19^{+0.18}_{-0.20}$ | $0.047^{+0.004}_{-0.004}$ |

In general, the synthetic FPS are consistent on large and intermediate scales ($0.003 \text{ s km}^{-1} \leq k \leq 0.04 \text{ s km}^{-1}$) with the estimates of Iršič et al. (2017), with minor differences on large scales in the case of $z = 3$ and $z = 3.2$. However, there are systematic discrepancies on the scales $k > 0.04$, where the models has less power than that from Iršič et al. (2017). This behaviour may suggest, that for the correct reproduction of the FPS it is necessary to use dataset, which coverings smaller scales.

On the other hand, the results show, that synthetic flux power spectrum is in good agreement with the high redshift measurements of $P(k)$ from the study of Boera et al. (2019). Also, the best-fit synthetic FPS shows good agreement with the large scale $P(k)$ with the results from eBOSS except of the redshifts $z = 3.2$, $z = 3.8$ and $z = 4.0$. Thus, such an approach can be also used for the cosmological parameter inference.

There is also limitation of lognormal seminumerical model, which is important to realize. The Jeans length depends on temperature and density, and therefore should be adaptive (Viel et al. 2002b). For the simplicity in this case, and also in most practical

implementations, it is assumed to be a constant. However, this leads to the equal smoothing of all dark matter structures independent of their density.

By comparing the lognormal model with the smooth particle hydrodynamical simulations, Arya et al. (2024) found that the lognormal model cannot simultaneously recover the true value values of all parameters. Since this failure mostly manifests in the poor recovery of Γ_{HI} , we use only 3-parameter fit.

Note that Arya et al. (2024) stated that four-parameter model $\{T_0, \gamma, x_J, \Gamma_{\text{HI}}\}$ is not a good description of baryonic density properties. This issue was slightly fixed by introducing another free parameter ν^1 to scale the 1D baryonic density field. However, in preliminary analysis we found that in some cases, especially when we cannot covers smaller scales ($k > 0.1$), this approach lead to the unstable results. This behaviour is demonstrated in Fig. 7, where we show parameter estimates obtained from the MCMC runs. These results show that the temperature at a mean density and the slope of the temperature-density relation corresponds to each other within the errors. However, in the case of x_J there is tendency to underestimate its value.

5.2. Evolution of the IGM Temperature

We also compared the obtained results with the predictions of 4 UVB models, namely the UVB model of Haardt & Madau (2012), Puchwein et al. (2019), Faucher-Giguère (2020) and the latter one with rescaled H I, He I, He II photoheating rates by a factor of 0.68. As shown in Gaikwad et al. (2021), this would results in a better match to the measured temperature evolution of the IGM at $z \geq 2$. The comparison of the IGM temperature evolution T_0 in the various models with the determined values is shown in Fig. 8. For this purpose, we used our temperature evolution code `TECO` (see Appendix B).

The comparison show that our results are consistent with the ones from Boera et al. (2019) and the UVB model of Faucher-Giguère (2020). However, the temperature at the mean density determined from the estimates of Iršič et al. (2017) is higher than predicted by various model. We identify two probable reasons for such behaviour. Firstly, we used only 30 lines of sight for the MCMC analysis. The second reason, which we believe was crucial, is that the data from Boera et al. (2019) covers smaller scales. This is demonstrated in Fig. 4, where the small differences in the FPS could be found at the scales $k > 0.1$. Additionally, we do not have a way to directly compare Jeans length x_J to any observations or simulations, since the lognormal uses a simplistic way to calculate baryonic density field. We found that our best-fit values of x_J are of the same order as obtained in Schaye (2001), assuming Ly α absorbers to be in hydrostatic equilibrium at $\sim 10^4$ K.

6. Conclusions

In this study, we used the lognormal seminumerical simulations of the Lyman α forest to determine the thermal parameters of the IGM. The main results could be summarized as follows:

1. The lognormal simulations can effectively recover temperature at mean density, slope of the temperature-density relation and Jeans length. Thus can be used for fast exploration of parameter space of thermal parameters T_0 , γ , and x_J .

¹ Note that we scales 1D baryonic density field before exponentiating in Eq. (10) according to $\delta_B(x, z) \rightarrow \nu \delta_B(x, z)$, which is the approach proposed by Arya et al. (2024).

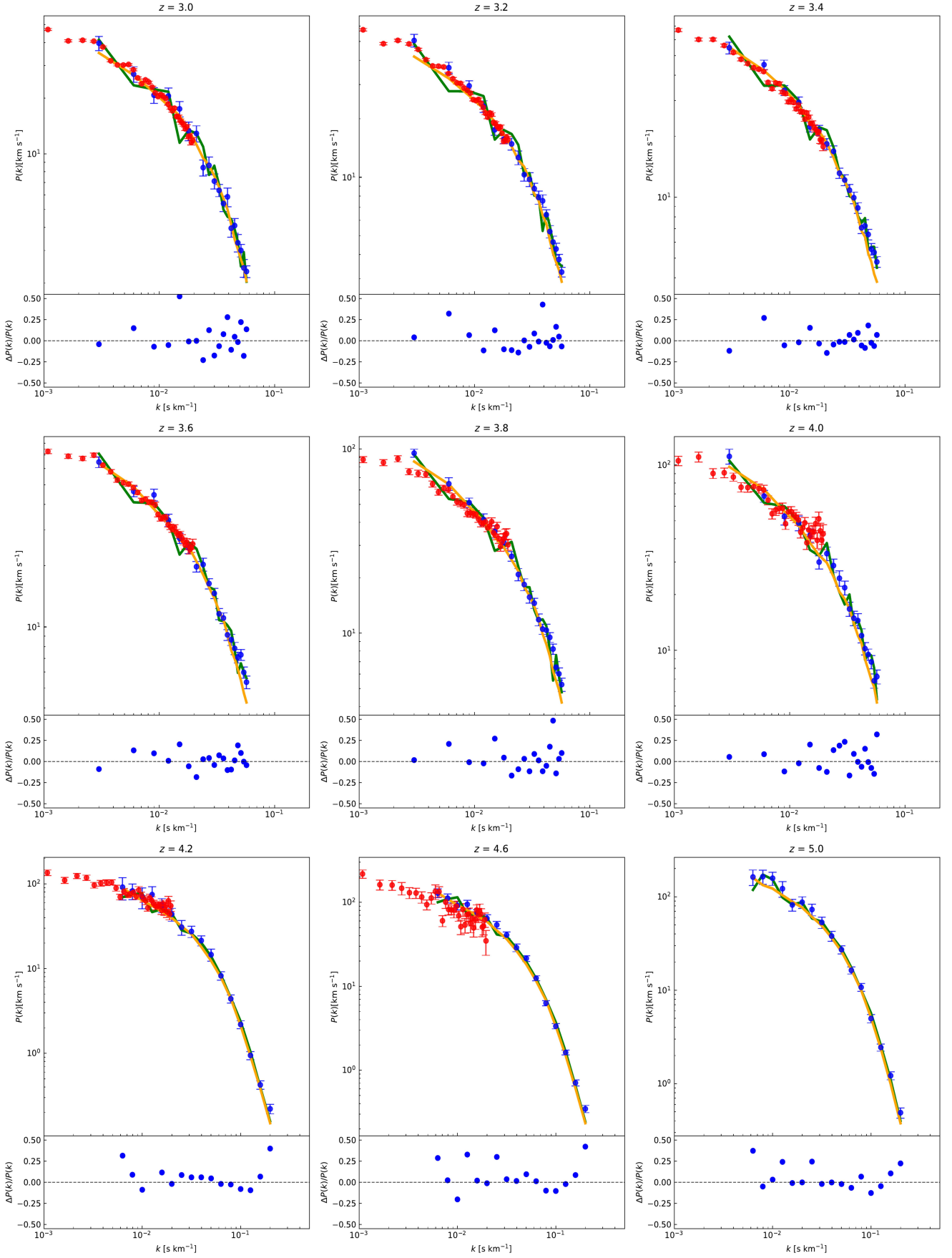


Fig. 6. $P(k)$ from the study of Boera et al. (2019) (blue points) and Chabanier et al. (2019) (red points), which were used to determine the parameters $\{T_0, \gamma$ and $x_j\}$. The best-fit evolutions of $P(k)$ based on the $N_{\text{LOS}} = 30$ and $N_{\text{LOS}} = 1000$ are shown with green and orange curves, respectively. The fractional differences of the observations and the best-fit model based on $N_{\text{LOS}} = 30$ are shown in the bottom part of each panel. Note that the differences from the eBoss measurements are not plotted.

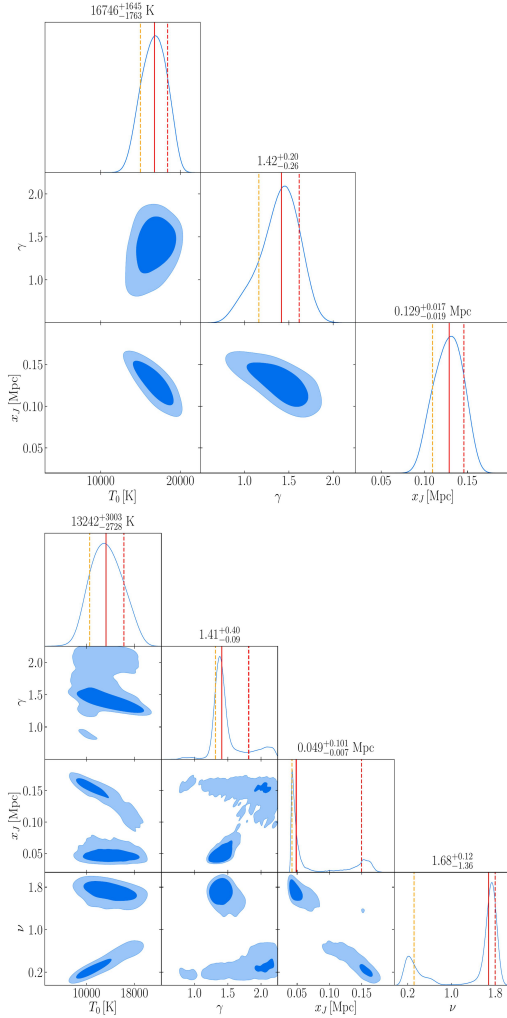


Fig. 7. Parameter estimates obtained from the MCMC runs in the 3D (top panel) and 4D (bottom panel) space for redshift $z = 3$. Red solid line corresponds to the median value and orange and red dashed lines correspond to the 16th and 84th percentile, respectively.

- Based on the comparison of synthetic flux power spectrum with determined one from eBOSS, it can be concluded that such an approach can be also used for the cosmological parameter inference.
- The synthetic FPS is consistent with the high redshift measurements of $P(k)$ of Boera et al. (2019). However, there is the difference when comparing to the estimates of Iršič et al. (2017), which was mainly caused by the lack of coverage on smaller scales $k > 0.1$.

These results also show that this approach is suitable for generating large number of synthetic spectra with input data and parameters. Therefore, it is ideal for interpreting the high-quality data obtained from the QSO absorption spectra surveys. In future work, we plan to prepare analysis pipeline for measuring the FPS, which uses the lognormal seminumerical simulations.

References

- Anninos, P., Zhang, Y., Abel, T., & Norman, M. L. 1997, *New Astronomy*, 2, 209
- Arya, B., Choudhury, T. R., Paranjape, A., & Gaikwad, P. 2023, *MNRAS*, 520, 4023
- Arya, B., Roy Choudhury, T., Paranjape, A., & Gaikwad, P. 2024, *J. Cosmology Astropart. Phys.*, 2024, 063

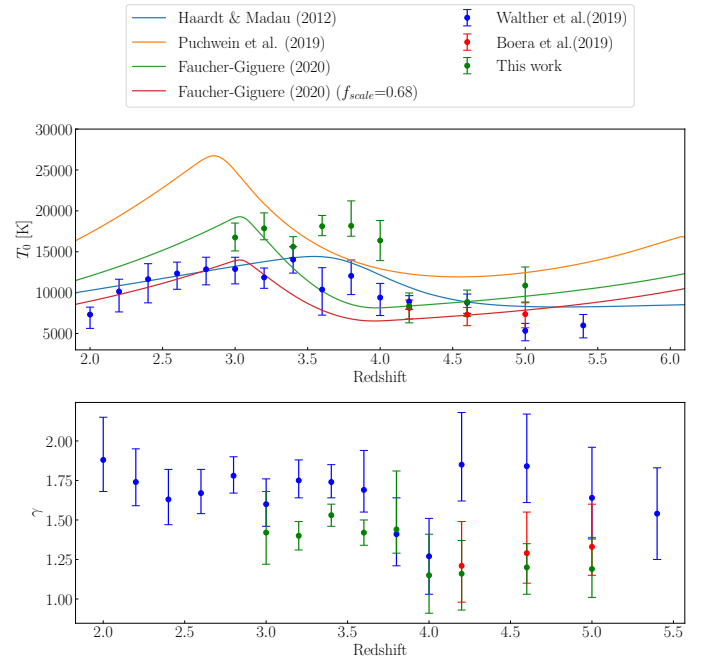


Fig. 8. Comparison of the results obtained in this study with various models. We also depict values, which were determined in Walther et al. (2019) and Boera et al. (2019).

- Bi, H. 1993, *ApJ*, 405, 479
- Bi, H. & Davidsen, A. F. 1997, *ApJ*, 479, 523
- Bi, H., Ge, J., & Fang, L.-Z. 1995, *ApJ*, 452, 90
- Bi, H. G., Boerner, G., & Chu, Y. 1992, *A&A*, 266, 1
- Boera, E., Becker, G. D., Bolton, J. S., & Nasir, F. 2019, *ApJ*, 872, 101
- Chabanier, S., Palanque-Delabrouille, N., Yèche, C., et al. 2019, *J. Cosmology Astropart. Phys.*, 2019, 017
- Choudhury, T. R., Srianand, R., & Padmanabhan, T. 2001, *ApJ*, 559, 29
- Coles, P. & Jones, B. 1991, *MNRAS*, 248, 1
- Croft, R. A. C., Weinberg, D. H., Bolte, M., et al. 2002, *The Astrophysical Journal*, 581, 20–52
- Demiański, M., Doroshkevich, A., Pilipenko, S., & Gottlöber, S. 2011, *MNRAS*, 414, 1813
- du Mas des Bourboux, H., Rich, J., Font-Ribera, A., et al. 2020, *ApJ*, 901, 153
- Faucher-Giguère, C.-A. 2020, *MNRAS*, 493, 1614
- Font-Ribera, A., McDonald, P., & Miralda-Escudé, J. 2012, *J. Cosmology Astropart. Phys.*, 2012, 017
- Gaikwad, P., Srianand, R., Haehnelt, M. G., & Choudhury, T. R. 2021, *MNRAS*, 506, 4389
- Gelman, A. & Rubin, D. B. 1992, *Statistical Science*, 7, 457
- Haardt, F. & Madau, P. 2012, *ApJ*, 746, 125
- Hui, L. & Gnedin, N. Y. 1997, *MNRAS*, 292, 27
- Iršič, V., Viel, M., Berg, T. A. M., et al. 2017, *MNRAS*, 466, 4332
- Katz, N., Weinberg, D. H., & Hernquist, L. 1996, *ApJS*, 105, 19
- Lewis, A. 2013, *Phys. Rev. D*, 87, 103529
- Lewis, A. & Bridle, S. 2002, *Phys. Rev. D*, 66, 103511
- Lewis, A., Challinor, A., & Lasenby, A. 2000, *ApJ*, 538, 473
- McDonald, P., Miralda-Escudé, J., Rauch, M., et al. 2000, *ApJ*, 543, 1
- McQuinn, M. & Upton-Sanderbeck, P. R. 2016, *MNRAS*, 456, 47
- Miralda-Escudé, J. & Rees, M. J. 1994, *MNRAS*, 266, 343
- Nagamine, K. 2018, *The Encyclopedia of Cosmology. Volume 2: Numerical Simulations in Cosmology*
- Petitjean, P., Mueket, J. P., & Kates, R. E. 1995, *A&A*, 295, L9
- Planck Collaboration, Ade, P. A. R., Aghanim, N., et al. 2014, *A&A*, 571, A16
- Puchwein, E., Haardt, F., Haehnelt, M. G., & Madau, P. 2019, *MNRAS*, 485, 47
- Rauch, M., Miralda-Escudé, J., Sargent, W. L. W., et al. 1997, *ApJ*, 489, 7
- Schaye, J. 2001, *arXiv e-prints, astro*
- Smith, B. D., Bryan, G. L., Glover, S. C. O., et al. 2017, *MNRAS*, 466, 2217
- Torrado, J. & Lewis, A. 2019, *Cobaya: Bayesian analysis in cosmology, Astrophysics Source Code Library, record ascl:1910.019*
- Torrado, J. & Lewis, A. 2021, *J. Cosmology Astropart. Phys.*, 2021, 057
- Viel, M., Matarrese, S., Mo, H. J., Haehnelt, M. G., & Theuns, T. 2002a, *MNRAS*, 329, 848
- Viel, M., Matarrese, S., Mo, H. J., Theuns, T., & Haehnelt, M. G. 2002b, *MNRAS*, 336, 685
- Viel, M., Weller, J., & Haehnelt, M. G. 2004, *MNRAS*, 355, L23
- Villasenor, B., Robertson, B., Madau, P., & Schneider, E. 2021, *ApJ*, 912, 912
- Villasenor, B., Robertson, B., Madau, P., & Schneider, E. 2022, *ApJ*, 933, 59
- Walther, M., Hennawi, J. F., Hiss, H., et al. 2018, *ApJ*, 852, 22
- Walther, M., Oñorbe, J., Hennawi, J. F., & Lukić, Z. 2019, *ApJ*, 872, 13

Appendix A: MCMC results

The parameter estimates obtained from the MCMC runs are presented in Fig. A.1.

Appendix B: Temperature evolution of the IGM

To derive the history of T_0 for various photoheating models, we solve the equation, which describe the temperature evolution of a Lagrangian fluid element at the cosmic mean density, i.e., with $\Delta = 1$ (Miralda-Escudé & Rees 1994; Hui & Gnedin 1997; McQuinn & Upton Sanderbeck 2016; Boera et al. 2019):

$$\frac{dT}{dt} = -2HT + \frac{2T}{3\Delta} \frac{d\Delta}{dt} - \frac{T}{\sum_i X_i} \frac{d\sum_i X_i}{dt} + \frac{2}{3k_B n_{\text{tot}}} \frac{dQ}{dt}, \quad (\text{B.1})$$

where d/dt is the Lagrangian derivative with respect to proper time, H is the Hubble parameter and n_b is the proper number density of all particles. The first term on the right-hand side takes into account cooling due to adiabatic expansion, while the second term gives adiabatic heating and cooling due to the structure formation. The thermal history at the mean density has been shown to depend weakly on this second term (McQuinn & Upton Sanderbeck 2016), therefore we ignored it in our calculation. The third term accounts for the change of internal energy per particle due to the change in the number of particles. The last term on the right-hand side of Eq.(B.1) describes the effect of heating and cooling rates and can be expanded as follows:

$$\frac{dQ}{dt} = \sum_X \frac{dQ_{\text{photo},X}}{dt} + \frac{dQ_{\text{Compton}}}{dt} + \sum_i \sum_X R_{i,X} n_e n_X, \quad (\text{B.2})$$

where $dQ_{\text{photo},X}/dt$ is the photoheating rate of ion $X = \{\text{H I}, \text{He I}, \text{He II}\}$, dQ_{Compton}/dt is the Compton cooling rate, and $R_{i,X}$ is the cooling rate coefficient for the ion X and cooling mechanism i (see Tab. 1 in the study by Katz et al. 1996). Besides, in the case of radiative cooling processes, we also include the inverse Compton cooling off the microwave background at the rate

$$\Lambda_C = 5.41 \times 10^{-36} n_e T (1+z)^4 [\text{erg s}^{-1} \text{cm}^{-3}] \quad (\text{B.3})$$

The number density of each species depends on the recombination and ionization rates. Therefore, we solve a kinetic network for the rate of change of species density n_i with the general form (Nagamine 2018):

$$\frac{\partial n_i}{\partial t} = \sum_j \sum_l k_{jl} n_j n_l + \sum_j I_j n_j, \quad (\text{B.4})$$

where k_{jl} is the rate for reactions involving species j and l and I_j is the appropriate radiative rate. This equation can be written schematically

$$\frac{\partial n_i}{\partial t} = C_i(T, n_j) - D_i(T, n_j) n_i, \quad (\text{B.5})$$

where C_i represents the total creation rate of species i (given the temperature T and other species densities) and D_i is the destruction rate of the same species, which must be proportional to n_i including both radiative and collisional processes (see Tab. 2 in the study by Katz et al. 1996). Due to the reproducibility, we describe the whole algorithm of calculation in Fig. B.1 and B.2. It is worth noting that for the calculation of the Eq. (B.5) we used the backwards difference formula (BDF) due to its stability (Smith et al. 2017). Discretization of Eq.(B.5) yields

$$n^{t+\Delta t} = \frac{C^{t+\Delta t} \Delta t + n^t}{1 + D^{t+\Delta t} \Delta t}. \quad (\text{B.6})$$

As noted in (Smith et al. 2017), the partial forwarding updating can be done by solving the various species in a specified order and using the updated species densities in the following partial step. In this work, we used the six species model: H I, H II, He I, He II, He III and e^- . This order was chosen based on the study by Anninos et al. (1997) and was determined through experimentalations.

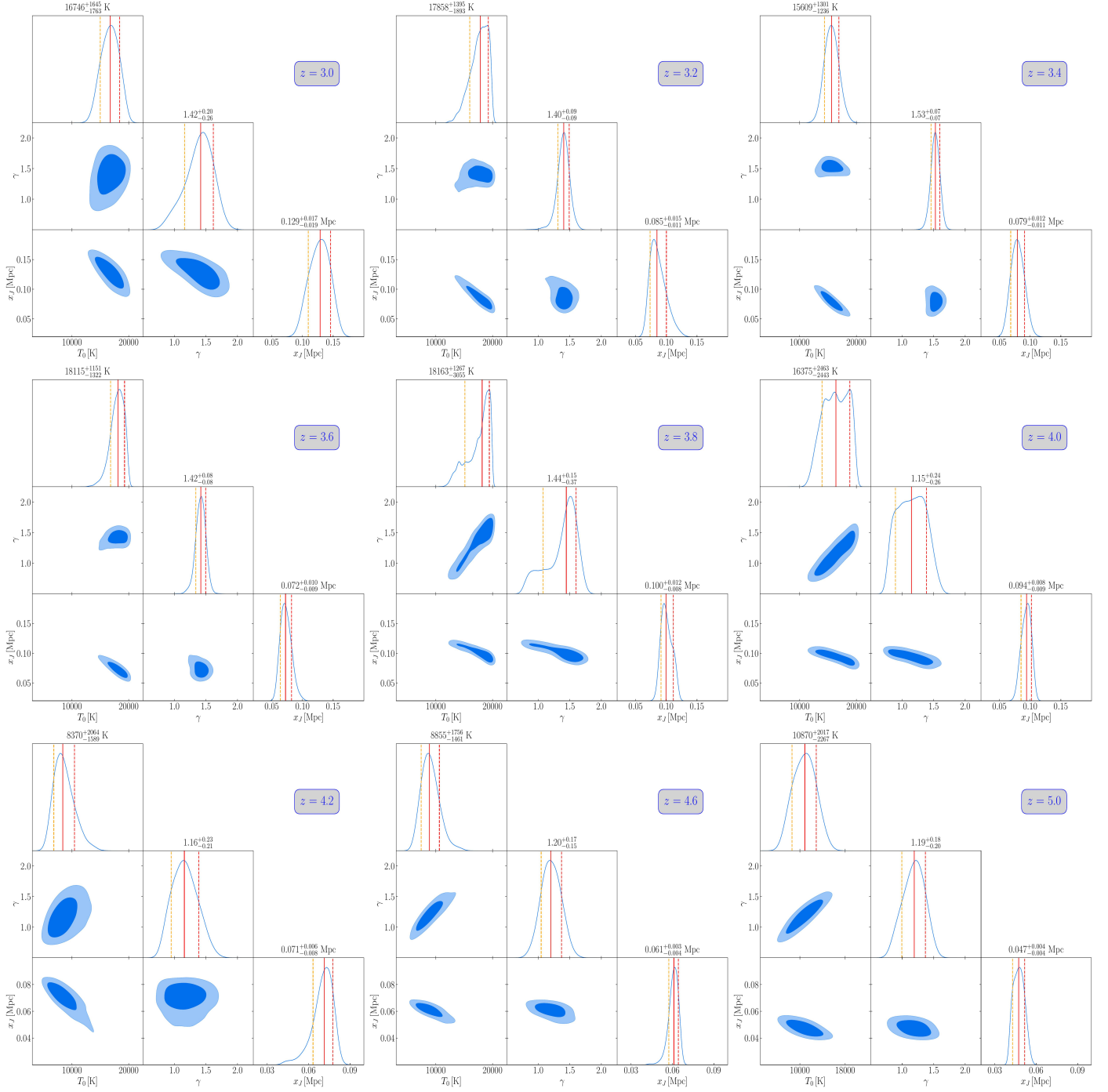


Fig. A.1. Parameter estimates obtained from the MCMC runs. Red solid line corresponds to the median value, orange and red dashed lines corresponds to the 16th and 84th percentile, respectively.

```

Input:  $z_{\text{start}}$  ;                                /* initial redshift */
 $z_{\text{end}}$  ;                                /* boundary value of redshift ( $z_{\text{end}} < z_{\text{start}}$ ) */
step ;                                /* step size of the calculation */
 $T_{\text{start}}$  ;                                /* initial value of temperature */
Treecool ;                                /* UVB TREECOOL file */
 $\Omega_{\Lambda}$  ;                                /* dark energy density */
 $\Omega_m$  ;                                /* matter density */
 $\Omega_b$  ;                                /* baryon density */
 $\Omega_k$  ;                                /* */
 $H_0$  ;                                /* Hubble constant in  $\text{s}^{-1}$  units */
 $Y$  ;                                /* primordial helium fraction by mass */

Output:  $z, T_0$ 

Constants:  $G = 6.6743 \times 10^{-8} \text{ cm}^3 \text{ g}^{-1} \text{ s}^{-1}$  ;                                /* gravitational constant */
 $m_p = 1.6726 \times 10^{-24} \text{ g}$  ;                                /* proton mass */
 $k_b = 1.3806 \times 10^{-16} \text{ erg K}^{-1}$  ;                                /* Boltzmann constant */

begin
   $z_{\text{values}} \leftarrow z_{\text{end}} : \text{step} : z_{\text{start}}$  ;                                /* creating evenly spaced sample which must be sorted in
    descending order */
   $a_{\text{values}} = 1/(z_{\text{values}} + 1)$  ;
   $\rho_c = (3H_0^2)/(8\pi G)$  ;
   $\bar{\rho}_{\text{gas}} = \Omega_b * \rho_c$  ;
   $n_{\text{HI}} = (1 - Y) * \bar{\rho}_{\text{gas}} / (m_p * a_{\text{values}}[1]^3)$  ;
   $n_{\text{HeI}} = Y * \bar{\rho}_{\text{gas}} / (4 * m_p * a_{\text{values}}[1]^3)$  ;
   $T_0[1] = T_{\text{start}}$  ;
   $n_{\text{HeII}}[1], n_{\text{HeIII}}[1], n_e[1] \leftarrow 0$  ;
  for  $i \leftarrow 2$  to  $\text{length}(a_{\text{values}})$  do
     $da = a_{\text{values}}[i] - a_{\text{values}}[i - 1]$  ;
     $H = H_0 * \sqrt{\Omega_M/a_{\text{values}}[i]^3 + \Omega_{\Lambda} + \Omega_k/a_{\text{values}}[i]^2}$  ;
     $\dot{a} = H_0 * \sqrt{\Omega_M/a_{\text{values}}[i] + \Omega_{\Lambda} * a_{\text{values}}[i]^2 + \Omega_k}$  ;
     $dt = da/\dot{a}$  ;
     $T_0[i], n_{\text{X}}[i] \leftarrow \text{call TECO-STEP}(T_0[i - 1], n_{\text{HI}}[i - 1], n_{\text{HeII}}[i - 1], n_{\text{HeI}}[i - 1], n_{\text{HeIII}}[i - 1],$ 
       $n_{\text{HeIII}}[i - 1], n_e[i - 1], dt; \text{Treecool}; z_{\text{values}}[i]; a_{\text{values}}[i], H )$  ;
  end
end

```

Fig. B.1. Algorithm of our temperature evolution code TECO.

Input: $T_0, n_{\text{HI}}, n_{\text{HII}}, n_{\text{HeI}}, n_{\text{HeII}}, n_{\text{HeIII}}, n_e; dt; \text{Treecool}; z; a; H$
Output: $T_0, n_{\text{HI}}, n_{\text{HII}}, n_{\text{HeI}}, n_{\text{HeII}}, n_{\text{HeIII}}, n_e$

```

begin
   $T_{0,\text{init}} \leftarrow T_0;$ 
   $n_{X,\text{init}} \leftarrow n_X;$ 
   $n_{\text{tot}} = n_{\text{HI}} + n_{\text{HII}} + n_{\text{HeI}} + n_{\text{HeII}} + n_{\text{HeIII}} + n_e;$ 
   $\Gamma_X \leftarrow \Gamma_X(z);$  /* returns interpolated value of  $\Gamma$  of species  $X = \{\text{HI}, \text{HeI}, \text{HeII}\}$  at
    specific redshift */
   $\mathcal{H}_X \leftarrow \mathcal{H}_X(z);$  /* returns interpolated value of  $\mathcal{H}$  of species  $X$  at specific redshift
    */
   $\mathcal{H}_{\text{tot}}(z) = \sum_X n_X * \mathcal{H}_X;$  /* returns the total value of  $\mathcal{H}$  of species  $X = \{\text{HI}, \text{HeI}, \text{HeII}\}$  */
   $RC_{\text{tot}} = \sum RC_X;$  /* sum of the recombination cooling rates */
   $CC_{\text{tot}} = \sum CC_X;$  /* sum of the collisional cooling rates */
   $FF \leftarrow \text{Eq. (23) from Katz et al.(1996)};$  /* free-free process */
   $\text{Compton} \leftarrow \text{Eq. (24) from Katz et al.(1996)};$ 
   $dQdt = \mathcal{H}_{\text{tot}} - RC_{\text{tot}} - CC_{\text{tot}} - FF - \text{Compton};$ 
   $\bar{\rho}_b = (n_{\text{HI}} + n_{\text{HII}} + 4 * (n_{\text{HeI}} + n_{\text{HeII}} + n_{\text{HeIII}})) * M_p;$ 
   $\tilde{X}_i = m_p * n_X / \bar{\rho}_b;$ 
   $\tilde{X}_{\text{tot}} = \tilde{X}_{\text{HI}} + \tilde{X}_{\text{HII}} + \tilde{X}_{\text{HeI}} + \tilde{X}_{\text{HeII}} + \tilde{X}_{\text{HeIII}} + \tilde{X}_e;$ 
   $C_{\text{HI}} = \alpha_{\text{HII}} * n_{\text{HII}} * n_e;$ 
   $D_{\text{HI}} = \Gamma_{\text{HI}} + \Gamma_{\text{eHI}} * n_e;$ 
   $n_{\text{HI}} = (C_{\text{HI}} * dt + n_{\text{HI}}) / (1 + D_{\text{HI}} * dt);$ 
   $C_{\text{HII}} = \Gamma_{\text{HI}} * n_{\text{HI}} + \Gamma_{\text{eHI}} * n_{\text{HI}} * n_e;$ 
   $D_{\text{HII}} = \alpha_{\text{HII}} * n_e;$ 
   $n_{\text{HII}} = (C_{\text{HII}} * dt + n_{\text{HII}}) / (1 + D_{\text{HII}} * dt);$ 
   $C_{\text{HeI}} = \alpha_{\text{HeII}} * n_{\text{HeII}} * n_e + \alpha_d * n_{\text{HeII}} * n_e;$ 
   $D_{\text{HeI}} = \Gamma_{\text{HeI}} + \Gamma_{\text{eHeI}} * n_e;$ 
   $n_{\text{HeI}} = (C_{\text{HeI}} * dt + n_{\text{HeI}}) / (1 + D_{\text{HeI}} * dt);$ 
   $C_{\text{HeII}} = \Gamma_{\text{HeI}} * n_{\text{HeI}} + \Gamma_{\text{eHeI}} * n_{\text{HeI}} * n_e + \alpha_{\text{HeIII}} * n_{\text{HeIII}} * n_e;$ 
   $D_{\text{HeII}} = \Gamma_{\text{HeII}} + \Gamma_{\text{eHeII}} * n_e + \alpha_{\text{HeII}} * n_e + \alpha_d * n_e;$ 
   $n_{\text{HeII}} = (C_{\text{HeII}} * dt + n_{\text{HeII}}) / (1 + D_{\text{HeII}} * dt);$ 
   $C_{\text{HeIII}} = \Gamma_{\text{HeII}} * n_{\text{HeII}} + \Gamma_{\text{eHeII}} * n_{\text{HeII}} * n_e;$ 
   $D_{\text{HeIII}} = \alpha_{\text{HeIII}} * n_e;$ 
   $n_{\text{HeIII}} = (C_{\text{HeIII}} * dt + n_{\text{HeIII}}) / (1 + D_{\text{HeIII}} * dt);$ 
   $C_e = \Gamma_{\text{HI}} * n_{\text{HI}} + \Gamma_{\text{HeI}} * n_{\text{HeI}} + \Gamma_{\text{HeII}} * n_{\text{HeII}} + \Gamma_{\text{eHI}} * n_{\text{HI}} * n_e + \Gamma_{\text{eHeI}} * n_{\text{HeI}} * n_e + \Gamma_{\text{eHeII}} * n_{\text{HeII}} * n_e;$ 
   $D_e = \alpha_{\text{HII}} * n_{\text{HII}} + \alpha_{\text{HeII}} * n_{\text{HeII}} + \alpha_d * n_{\text{HeII}} + \alpha_{\text{HeIII}} * n_{\text{HeIII}};$ 
   $n_e = (C_e * dt + n_e) / (1 + D_e * dt);$ 
   $d\tilde{X}dt = m_p * (C_e - D_e * n_e) / \bar{\rho}_b;$ 
   $T_0 = T_{0,\text{init}} - 2 * H * T_{0,\text{init}} * dt + (2 * dQdt / (3 * k_b * n_{\text{tot}})) * dt - (T_{0,\text{init}} * d\tilde{X}dt / \tilde{X}_{\text{tot}}) * dt;$ 
   $n_X = n_X - 3 * H * n_{X,\text{init}} * dt;$ 
end

```

Fig. B.2. Algorithm of the TECO-STEP.